

How does a newly-formed drainage divide migrate after a river capture event? Insights from numerical simulations and two natural cases (Yarlung-Yigong, and Dadu-Anning) in the Tibetan Plateau region

Shuang Bian¹, Xibin Tan², Chao Zhou³, Feng Shi⁴, and Yiduo Liu²

¹Institute of Geology, China Earthquake Administration

²Institute of Mountain Hazards and Environment, Chinese Academy of Sciences

³State Key Laboratory of Earthquake Dynamics, Institute of Geology, China Earthquake Administration

⁴State Key Laboratory of Earthquake Dynamics, Institute of Geology, China Earthquake Administration, Beijing 100029, China.

November 8, 2023

Abstract

Tectonic and/or climatic perturbations can drive drainage adjustment. The capture events, significantly changing the river network topology, are the major events in river network evolution. While they could be identified through field observations and provenance analysis, reconstructing this evolution process and pinpointing the capture time remain challenging. Following a capture event, the steady-state elevation of the captor river will be much lower than that of the beheaded river. Then, the newly-formed drainage divide will migrate towards the beheaded river, a process also known as river-channel reversal. The migration of the newly-formed drainage divide provides a new perspective for identifying the reorganization of the river network. Here, we employ numerical modeling to reproduce the characteristic phenomena of drainage-divide migration following capture events and analyze the effects of different parameters on the migration rate. We find that (1) the migration of newly-formed drainage divides can last for tens of millions of years, with the migration rate decreasing exponentially over time; (2) larger captured area, higher uplift rate, and lower erosional coefficient, all of which cause a higher cross-divide difference in steady-state elevation, will cause higher migration rate of the newly-formed drainage divide. This insight was further applied to the Dadu-Anning and Yarlung-Yigong capture events. We predict the present Dadu-Anning drainage divide would further migrate ~65–92 km southward to reach a steady state in tens of millions of years. The Yarlung-Yigong capture event occurred in the early-middle Cenozoic, which implies that the late-Cenozoic increased exhumation rate is not related to the capture event.

Hosted file

977872_0_art_file_11531854_s36vpd.docx available at <https://authorea.com/users/695108/articles/683939-how-does-a-newly-formed-drainage-divide-migrate-after-a-river-capture-event-insights-from-numerical-simulations-and-two-natural-cases-yarlung-yigong-and-dadu-anning-in-the-tibetan-plateau-region>

Hosted file

977872_0_supp_11531857_s36v4h.docx available at <https://authorea.com/users/695108/articles/683939-how-does-a-newly-formed-drainage-divide-migrate-after-a-river-capture-event->

insights-from-numerical-simulations-and-two-natural-cases-yarlung-yigong-and-dadu-
anning-in-the-tibetan-plateau-region

Hosted file

977872_0_supp_11531856_s36v4m.gif available at <https://authorea.com/users/695108/articles/683939-how-does-a-newly-formed-drainage-divide-migrate-after-a-river-capture-event-insights-from-numerical-simulations-and-two-natural-cases-yarlung-yigong-and-dadu-anning-in-the-tibetan-plateau-region>

1 **How does a newly-formed drainage divide migrate after a river**
2 **capture event? Insights from numerical simulations and two natural**
3 **cases (Yarlung-Yigong, and Dadu-Anning) in the Tibetan Plateau**
4 **region**

5

6 **Shuang Bian¹, Xibin Tan^{2,*}, Chao Zhou¹, Feng Shi¹, Yiduo Liu²**

7 ¹ State Key Laboratory of Earthquake Dynamics, Institute of Geology, China

8 Earthquake Administration, Beijing 100029, China

9 ² Key Laboratory of Mountain Hazards and Surface Processes, Institute of Mountain

10 Hazards and Environment, Chinese Academy of Sciences, Chengdu 610041, China

11

12 *Corresponding author: Xibin Tan

13 E-mail address: tanxibin@imde.ac.cn

14

15 **Key Points:**

16 • A newly-formed drainage divide following a capture event migrates for tens of
17 millions of years, with a decreasing rate over time.

18 • The Dadu-Anning drainage divide would further migrate ~65–92 km
19 southward to reach a steady state in tens of millions of years.

20 • The Yarlung-Yigong capture event occurred in the early-middle Cenozoic,
21 which cannot drive the late-Cenozoic enhanced exhumation.

22 **Abstract**

23 Tectonic and/or climatic perturbations can drive drainage adjustment. The
24 capture events, significantly changing the river network topology, are the major
25 events in river network evolution. While they could be identified through field
26 observations and provenance analysis, reconstructing this evolution process and
27 pinpointing the capture time remain challenging. Following a capture event, the
28 steady-state elevation of the captor river will be much lower than that of the beheaded
29 river. Then, the newly-formed drainage divide will migrate towards the beheaded river,
30 a process also known as river-channel reversal. The migration of the newly-formed
31 drainage divide provides a new perspective for identifying the reorganization of the
32 river network. Here, we employ numerical modeling to reproduce the characteristic
33 phenomena of drainage-divide migration following capture events and analyze the
34 effects of different parameters on the migration rate. We find that (1) the migration of
35 newly-formed drainage divides can last for tens of millions of years, with the
36 migration rate decreasing exponentially over time; (2) larger captured area, higher
37 uplift rate, and lower erosional coefficient, all of which cause a higher cross-divide
38 difference in steady-state elevation, will cause higher migration rate of the
39 newly-formed drainage divide. This insight was further applied to the Dadu-Anning
40 and Yarlung-Yigong capture events. We predict the present Dadu-Anning drainage
41 divide would further migrate ~65–92 km southward to reach a steady state in tens of
42 millions of years. The Yarlung-Yigong capture event occurred in the early-middle

43 Cenozoic, which implies that the late-Cenozoic increased exhumation rate is not
44 related to the capture event.

45 **Plain Language Summary**

46 A capture event will lead to the formation of a new drainage divide between the
47 capture point and the beheaded river. Then, the newly-formed drainage divide will
48 migrate towards the beheaded river, a process called river-channel reversal. In this
49 study, we used numerical modeling and natural examples to explore how a
50 newly-formed drainage divide migrate after a river capture event. We find that the
51 migration of newly-formed drainage divides can last for tens of millions of years, and
52 the migration rate decreases exponentially over time. In addition, a larger captured
53 area, higher uplift rate, or lower erosional coefficient can enhance the migration of the
54 newly-formed drainage divide. We further applied our modeling to two natural
55 examples. Our results show that the present Dadu-Anning divide is moving south and
56 this process would last for tens of millions of years. The Parlung River has reversed
57 its flow direction for over 200 km and reached a new steady state, which means an
58 early formation of the modern Yarlung River, rather than the hypothetical Quaternary
59 capture event of the Parlung River.

60 **1 Introduction**

61 The landscape equilibrium state can be upset by tectonic and/or climatic
62 disturbances, as they alter the steady-state elevation of river channels (Whipple, 2001).
63 When two river channels sharing a drainage divide have different steady-state
64 elevations at their channel heads, the drainage divide will migrate toward the victim
65 side with a higher steady-state elevation (Willett et al., 2014). The divide migration
66 process will simultaneously decrease and increase the steady-state elevation of the
67 victim and aggressor side, respectively, until the cross-divide difference is eliminated
68 (Willett et al., 2014). The divide then reaches a new steady state and adapts to the new
69 tectonic and climatic environment (He et al., 2021; Shi et al., 2021; Zhou et al.,
70 2022a).

71 Contrary to continuous divide migration, discrete river capture events make a
72 substantial adjustment in river network topology around the capture point (Morisawa,
73 1989; Bishop, 1995; Clark et al., 2004; Prince et al., 2011; Yanites et al., 2013; Lave,
74 2015; Stokes et al., 2018; Yang et al., 2020), and thus can rapidly change the
75 steady-state elevation on both sides of the newly-formed drainage divide (Bishop,
76 1995; Goren et al., 2014; Willett et al., 2014; Shelef and Goren, 2021). As river
77 capture events impact the evolution of the landscape, ecosystem, and even human
78 civilizations (Winemiller et al., 2008; Willis et al., 2010; Hoorn et al., 2010; Xing et
79 al., 2017), how and when they occurred is one of the major concerns for earth
80 scientists (e.g., Clark et al., 2004; Fan et al., 2018; Yang et al., 2020). However, most
81 capture events in case study remain controversial on their detailed processes and

82 occurring time (Clark et al., 2004; Cina et al., 2009; Lang and Huntington, 2014;
83 King et al., 2016; Gourbet et al., 2017; Govin et al., 2018; Zhang et al., 2019; Zhao
84 et al., 2021a, b).

85 Past river capture events could be inferred from barbed tributaries, wind gaps,
86 abandoned river channels, paleocurrent direction, and provenance analysis (Bishop,
87 1995; Clark et al., 2004; Brocard et al., 2011; Zhang et al., 2012; Bracciali et al., 2015;
88 Chen et al., 2017; Fan et al., 2018, 2021; Harel et al., 2019; Xie et al., 2020; Yang et
89 al., 2021; Zhao et al., 2021a, b). However, to obtain the exact time of dating the
90 capture event is more challenging based upon these methods. This is partially because
91 only the river relict sediments before the capture event can record the paleocurrent
92 direction and provide a constraint on the capture event timing. A capture event usually
93 occurred several or even tens of millions of years ago. It is not easy to find the
94 paleochannel sediments on the main trunk of the beheaded, or the reversal and captor
95 rivers (Clark et al., 2004; Fan et al., 2010, 2018; Wei et al., 2016), even though the
96 sediments usually only provide an upper or lower limit to the capture time.

97 One way to study the river capture process, circumventing the caveats in the
98 conventional, sediment-based techniques, is via the analysis of drainage divides.
99 Immediately after a capture event, the steady-state elevation of the captor river is
100 much lower than that of the beheaded river, which can cause a new and greater
101 disequilibrium. Then, the newly-formed drainage divide will migrate from the capture
102 point towards the beheaded-river side, which results in a small, but significant
103 phenomenon called *river-channel reversal* (Clark et al., 2004; Clift et al., 2006; Harel

104 [et al., 2019](#); [Yang et al., 2020](#); [Shelef and Goren, 2021](#); [Zeng and Tan, 2023](#)).
105 Therefore, the location and the stability of drainage divides, especially the
106 newly-formed drainage divide between the reversal and the beheaded river channels,
107 could provide new and independent constraints on the processes and time scales of the
108 capture event.

109 In this study, we first use numerical modeling to explore the dynamics of river
110 capture events and analyze the effects of captured area, uplift rate, and erosional
111 coefficient on the migration rate of the newly-formed drainage divide. Then, we
112 present two natural cases with significant river capture events, the Dadu-Anning in
113 eastern Tibet and the Yarlung-Yigong in the eastern Himalayan syntaxis region to
114 show how the modeling results are used to constrain the occurring time of capture
115 events.

116 **2 Background**

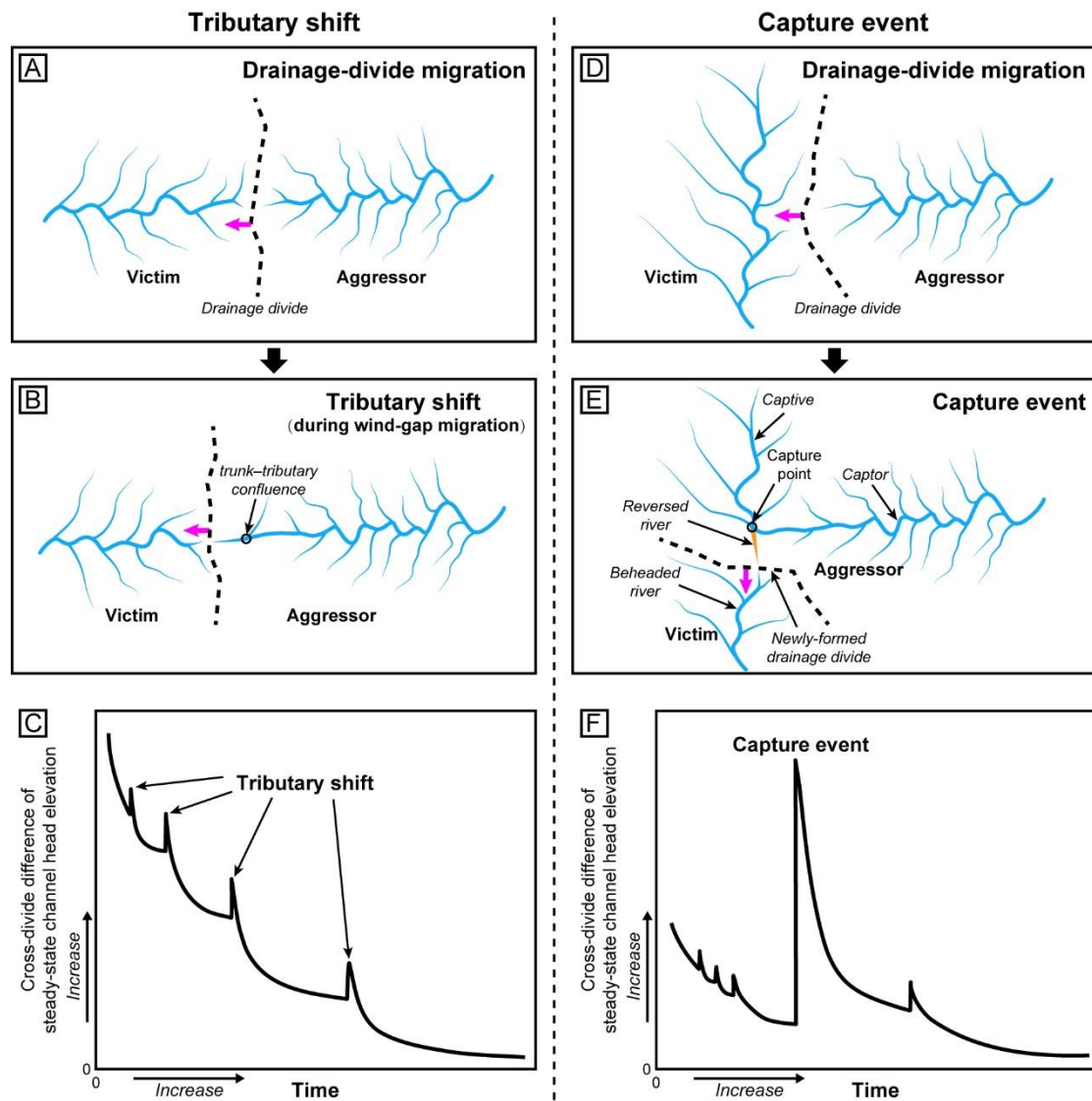
117 To frame our analysis, we first make a conceptual overview of the river capture
118 event. We then summarize analytical models of steady-state elevation at the channel
119 heads. In addition, we briefly review the background on the Dadu-Anning and
120 Yarlung-Yigong capture events, which are two typical natural cases of river capture
121 on the Tibetan Plateau.

122 **2.1 River capture event**

123 River capture is a more common natural process with the interception of a river
124 by an adjacent river as mountainous landscapes evolve ([Bishop, 1995](#)). So far, most

125 identified river captures occurred between two tributaries with relatively small
126 drainage areas (usually several to hundreds of square kilometers), accompanied by
127 wind-gap migration (Shelef and Goren, 2021). This process is termed *tributary shift*
128 here (Figs. 1B). As the divide migrates across these trunk-tributary confluences, the
129 ongoing tributary shift towards the aggressor side causes slight fluctuations in the
130 cross-divide difference in steady-state elevation (Fig. 1C).

131 On the other hand, a more severe scenario exists, in which a river captures a vast
132 area (such as thousands of square kilometers or greater) all at once by cutting the
133 trunk of the other river. Such a catastrophic process is called *capture event*, and is
134 usually regarded as the landmark of river network reorganization (Figs. 1D-E). A
135 capture event reduces the steady-state elevation of the captor river by increasing the
136 upstream area and raises the steady-state elevation of the beheaded river by
137 decreasing the upstream area (Willett et al., 2014; Yang et al., 2015; Whipple et al.,
138 2017). Therefore, a capture event makes a significant cross-divide steady-state
139 elevation contrast (Fig. 1F). In this study, we focus primarily on the capture events.
140



141

142 **Fig. 1** Schematic illustration of tributary shift (A, B, C) and capture event (D, E, F). (A-B) A
 143 typical drainage-divide migration process with gradual shifts between tributaries. (C) The
 144 change of the cross-divide difference of steady-state channel-head elevation over time during
 145 the tributary shift process. The tributary shift can cause fluctuations in the cross-divide
 146 difference in steady-state elevation. (D-E) Illustrations of a significant drainage system
 147 reorganization after a capture event. Note the sudden, remarkable change in the river network.
 148 (F) The change of the cross-divide difference in steady-state channel-head elevation over time
 149 during the capture event. The capture event significantly increases the cross-divide difference
 150 of steady-state elevation.

151 2.2 Steady-state elevation and steady-state channel profile

152 Steady-state elevation is a theoretical value for which erosion would balance
153 rock uplift (Whipple, 2001). It can be estimated from the model for river incision into
154 bedrock (Whipple, 2001; Willett et al., 2014). According to the detachment-limited
155 stream power model (Howard and Kerby, 1983), the erosion rate (E) is usually
156 expressed as the following:

$$157 \quad E = KA^m S^n \quad (2)$$

158 where K is the erosion coefficient, S is the channel gradient, A is the upstream area,
159 and m and n are the area and slope exponents, respectively. At a steady state ($E = U$, U
160 is uplift rate), Eq. (2) can be solved for the following expression (Kirby and Whipple,
161 2001):

$$162 \quad S = \left(\frac{U}{K}\right)^{\frac{1}{n}} A^{-\frac{m}{n}} \quad (3)$$

163 The steady-state solution of a river channel profile (z) can be derived from integrating
164 the channel distance (x):

$$165 \quad z(x) = z_b + \int_{x_b}^x \left(\frac{U}{K}\right)^{\frac{1}{n}} A(x)^{-\frac{m}{n}} dx \quad (4)$$

166 where z_b is the elevation at the river base point. Parameter χ was introduced as an
167 integral function of position in the river channel (Perron and Royden, 2013):

$$168 \quad \chi = \int_{x_b}^x \left(\frac{A_0}{A(x)}\right)^{\frac{m}{n}} dx \quad (5)$$

169 where A_0 is an arbitrary scaling area to make the integrand dimensionless. Then, the
170 steady-state solution of a river channel profile (z) can be expressed as:

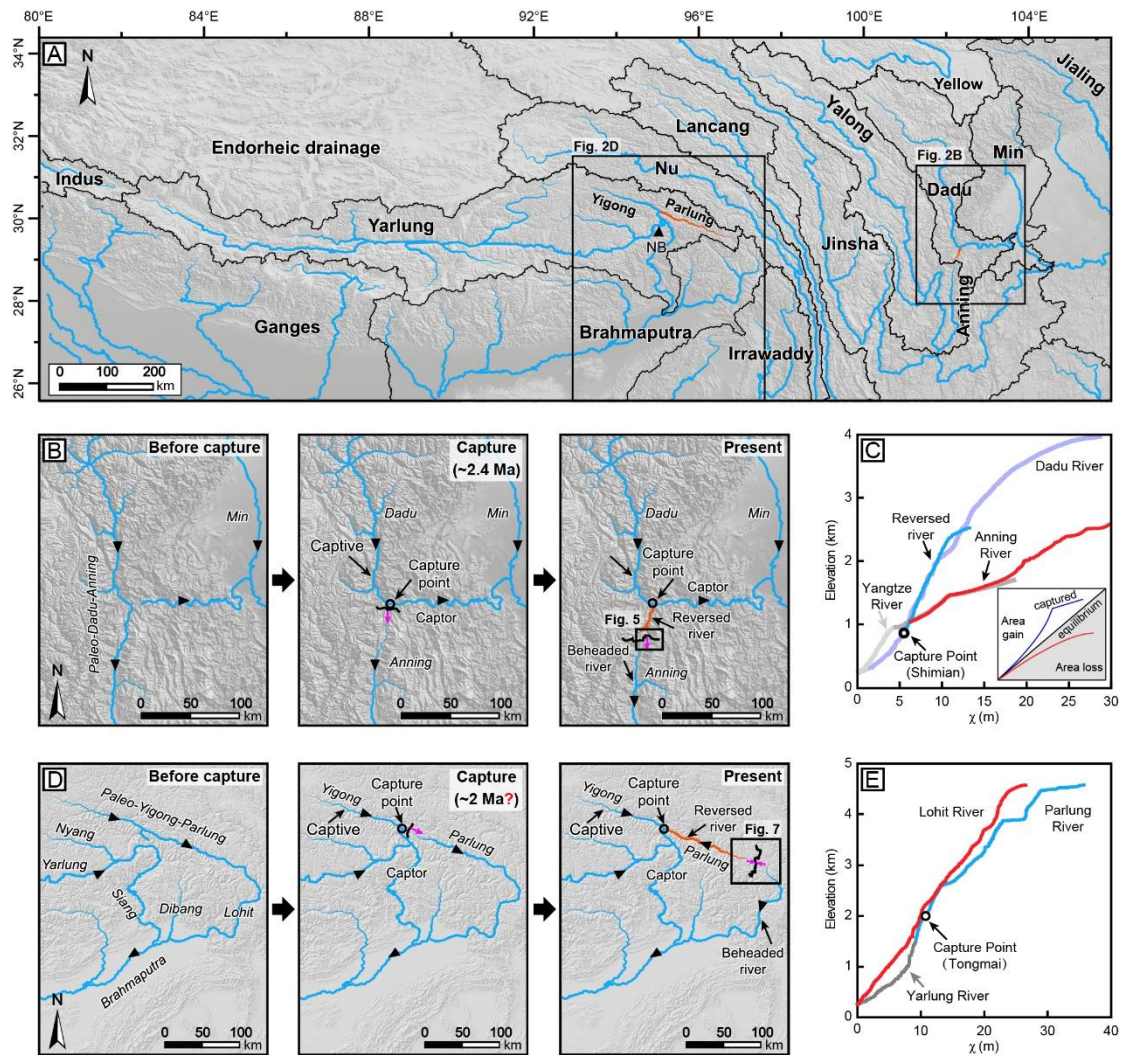
$$171 \quad z(x) = z_b + \left(\frac{U}{K}\right)^{\frac{1}{n}} (A_0)^{-\frac{m}{n}} \chi \quad (6)$$

172

173 2.3 Background on the Dadu-Anning capture event

174 The Dadu River, located in the eastern Tibetan Plateau, is a major tributary of the
175 Yangtze River (Figs. 2A-B). It flows >600 km southwards from the Songpan-Ganze
176 Terrane, and then makes an abrupt ($\sim 90^\circ$) loop at the town of Shimian, turning
177 eastward into the Sichuan Basin. To the south of this river bend, a low and wide pass
178 (wind gap) separates the Dadu River from the south-flowing Anning River. The
179 Anning River drains a broad alluvial valley and finally converges with the Yangtze
180 River (Fig. 2A). On the χ -plot (Fig. 2C), the Dadu River shows a high channel
181 steepness in the middle reaches and less steep profiles in its upper and lower reaches,
182 while the Anning River shows a gentle upper reach, and becomes steeper in its lower
183 reach.

184 This river network pattern is suggested as a consequence of a capture event
185 between the Dadu and Anning Rivers, based on the topography map, the existence of
186 the wind gap, and fluvial sediments preserved within it (Clark et al., 2004; Yang et al.,
187 2020; Zheng et al., 2023). The paleo-Dadu-Anning River originally flowed southward,
188 and then was captured by an east-flowing paleo-Dadu River (Fig. 2B). The capture
189 event formed the present Dadu River and beheaded the Anning River (“Anning”
190 means quiet in Chinese). The newly-formed Dadu-Anning drainage divide was
191 located close to the capture point (Shimian) and started to migrate southward (Fig.
192 2B). Yang et al. (2020) assigned this capture event at ~ 2.4 Ma based on provenance
193 analysis, thermochronometry, topographic analysis, and numerical modeling.



194

195 **Fig. 2** (A) Overview of the major rivers and drainage basins in the Tibetan Plateau and
 196 surrounding region. (B) Illustration of the Dadu-Anning capture event. (C) χ -plots for the
 197 Dadu and Anning Rivers. (D) Illustration of the Yarlung-Parlung capture event. (E) χ -plots
 198 for the Parlung and Lohit Rivers.

199 2.4 Background on the Yarlung-Yigong capture event

200 In the eastern Himalayan orogenic belt, two major rivers, the southeast-flowing
 201 Yigong and northwest-flowing Parlung Rivers, incised the Namche Barwa massif and
 202 connected with the Siang River through the Tsangpo Gorge (**Fig. 2A**). After the
 203 confluence of the Siang, Dibang and Lohit Rivers, it becomes the Brahmaputra River.
 204 Along the Parlung River, all the barbed tributaries, wind gaps, and the low drainage

205 divide indicated that it has experienced river capture and reversal (Burchfiel et al.,
206 2000; Clark et al., 2004; Seward and Burg, 2008; King et al., 2016; Yang et al., 2021).

207 Two end-member models have been proposed to explain the complex drainage
208 pattern. Some authors suggested that the Yarlung River once flowed east into the
209 Irrawaddy River through the Parlung River, which was sequentially captured by
210 headward erosion of the Siang-Brahmaputra (Burchfiel et al., 2000; Clark et al., 2004;
211 Robinson et al., 2014). Others postulated a paleo-Yigong-Parlung-Lohit River, with
212 the capture of an antecedent Yarlung-Siang-Brahmaputra River (Seward and Burg,
213 2008; Lang and Huntington, 2014; Govin et al., 2018). Regardless of the method of
214 capture, the reversal of the Parlung River first occurs at the present Yigong-Parlung
215 confluence (the town of Tongmai), and then the newly-formed drainage divide moves
216 eastward to its current position (Fig. 2C). The headwaters of the Parlung River are
217 separated from the Lohit River by the Parlung-Lohit drainage divide.

218 **3 Numerical modeling on landscape evolution**

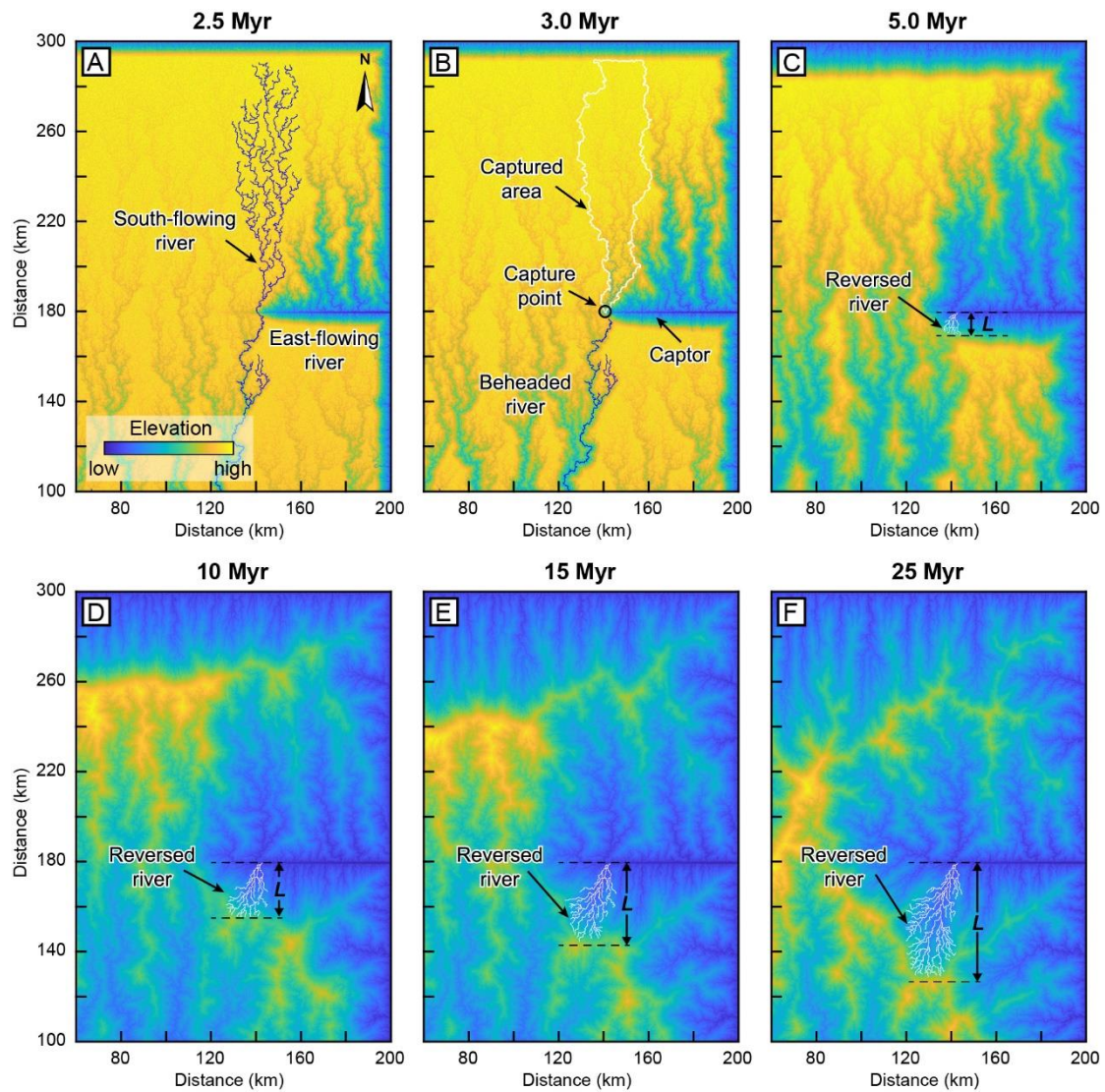
219 To explore the dynamics of river capture event and its control factors, we
220 performed 10 numerical experiments using the TopoToolbox Landscape Evolution
221 Model (Campforts et al., 2017). In addition, we further analyzed the effects of
222 captured area, uplift rate, and erosional coefficient on the location and migration rate
223 of the newly-formed drainage divide.

224 **3.1 Reference Model**

225 We first conduct a landscape evolution modeling to reproduce the evolution of
226 the newly-formed drainage divide migration after a river capture event. The reference
227 model (Fig. 3) extends 200 km long in the E-W direction and 300 km wide in the N-S

228 direction, which is resolved by a spatial resolution of 100 m. The initial elevation is
229 set as a constant elevation of 1000 m on the northern edge, whereas the elevation at
230 the southern edge is fixed to 0 m. The uplift rate is uniform across the model domain
231 (3 mm/yr) except for a narrow zone in the east-central part of the model ($X = 140\text{--}200$
232 km; $Y = 179\text{--}180$ km), in which an eastward decreasing gradient zone of uplift rate is
233 assigned to simulate an originally east-flowing river. Other model parameters in the
234 reference model are set as follows: erosional coefficient (K) is 2×10^{-6} /year; area
235 exponent (m), 0.5; slope exponent (n), 1; hillslope diffusivity, $0.03 \text{ m}^2/\text{year}$; and
236 drainage area threshold, 0.1 km^2 . The model was run for over 30 Myr, with a time step
237 of 0.5 Myr (Movie S1).

238 **Figure 3** shows selected representative snapshots of the reference model. At the
239 initial stage, the drainage system contains a major, south-flowing river and a local,
240 east-flowing river on the asymmetrically uplifted slope (Fig. 3A). Subsequently, the
241 east-flowing river captures the south-flowing rivers, generating a new segment of the
242 drainage divide between the reversal and the beheaded channels at the capture point
243 (Fig. 3B). Due to this capture event, the area gain for the captor rivers increases the
244 headwater channel steepness, and in turn leads to a fast erosion rate. In contrast, the
245 beheaded river loses the upstream area, leading to a corresponding decrease in
246 channel steepness and erosion rate. The cross-divide difference in erosion rate further
247 drives the newly-formed drainage divide to migrate southward (Figs. 3C-D). As the
248 divide migrates, the reversal river channel is elongated and the beheaded river channel
249 shrinks. This results in an overall increase in the channel gradient of the beheaded
250 river drainage compared to the reversal river drainage, and thus the drainage-divide
251 migration rate slows down over time (Figs. 3D-F) (Braun, 2017; Whipple et al., 2017;
252 Shelef and Goren, 2021).



253

254 **Fig. 3** Numerical landscape evolution model in response to a capture event. (A) The initial
 255 drainage system developed several south-flowing rivers and east-flowing rivers on the
 256 asymmetrically uplifted slope. (B) The originally south-flowing rivers are captured and turn
 257 to flow eastward. A new east-trending drainage divide was formed close to the capture point.
 258 (C-F) The newly-formed divide continues to migrate southward, resulting in an extension of
 259 the reversal channel. L represents the reversal distance, which refers to the vertical distance
 260 from the divide to the main trunk.

261 2.2 Effects of captured area

262 During the drainage-divide migration process, a river capture event

263 instantaneously alters the drainage area, that is, the drainage area is removed from the
264 beheaded and added to the captor rivers. This process leads to a change in the
265 steady-state elevation of channel heads across the newly-formed drainage divide (Fig.
266 1F), which further promotes the drainage divide to migrate towards the
267 beheaded-river side (Willett et al., 2014; Whipple et al., 2017; Shelef and Goren, 2021;
268 Ye et al., 2022). To delineate the effect of the captured area on the migration of the
269 newly-formed drainage divide, we systematically varied the size of the captured area
270 by proportionally enlarging the model domain (Figs. 4A-B; Supplementary Fig. S1).
271 Other parameters remained the same as the reference model.

272 We first obtained the location of the newly-formed drainage divide at each
273 moment (at a time step of 0.5 Myr). The distance between the drainage divide and the
274 main trunk of the east-flowing river is called *river-channel reversal distance* (Fig. 3).
275 We measured the reversal distance at 2 Myr intervals (Fig. 4A), and calculated the
276 mean reversal rate (Fig. 4B). The mean reversal rate, V , can be estimated by the
277 equation of $V = (L_2 - L_1) / (t_2 - t_1)$, where L_2 and L_1 are the reversal distances at two
278 instants of t_2 and t_1 , respectively. Here, we obtained the mean reversal rate every 2
279 Myr (i.e., $t_2 - t_1$), except for a rate at the very beginning with the interval of 1 Myr.

280 Under different scenarios, the reversal rates exhibit similar trends, in which the
281 value is the greatest in the early stage, exponentially decreases to half after ~2–3 Myr,
282 and further declines smoothly towards zero in the following tens of millions of years
283 (Fig. 4B). In addition, the reversal rate and reversal distance increase with increasing
284 captured area. When the captured area is set to ~2,200 km², the reversal rate is ~7.5
285 mm/yr at the very beginning of the experiment (1 Myr) and then gradually slows
286 down (Fig. 4B). In this case, the drainage divide has migrated ~60 km within ~20 Myr
287 (Fig. 4A). When the captured area is increased to ~25,000 km², the reversal distance

288 is rapidly built up within the first ~8 Myr. The reversal rate in the early stage can
289 reach the peak value of ~18 mm/yr, which is greater than those in other models.

290 **2.3 Effects of uplift rate**

291 Drainage adjustment is strongly controlled by vertical tectonic movement
292 (Mitchell and Yanites, 2019; He et al., 2019; Shi et al., 2021; Ye et al., 2022), which
293 can be represented by various uplift rates in this circumstance. To test the effects of
294 tectonic on the migration rate of the newly-formed drainage divide, we assigned
295 various uplift rates of 1, 2, 3, and 4 mm/yr (Figs. 4C-D) for model runs. The size of
296 the captured area is constrained within a 10% error range with the reference model.
297 The landscape evolution processes (Supplementary Fig. S2) are comparable to the
298 reference model.

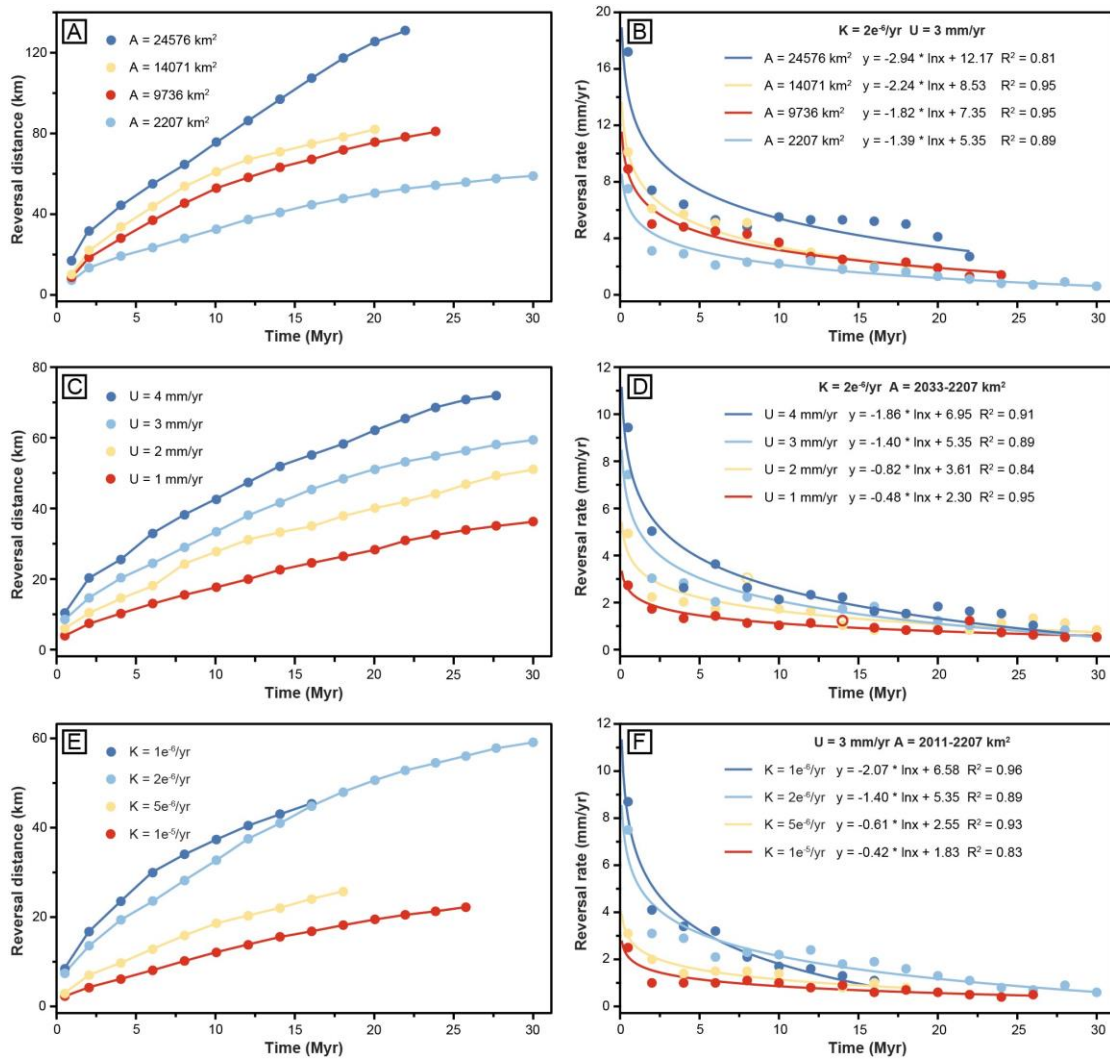
299 All the model results demonstrate that the newly-formed drainage divide after a
300 capture event migrates southward for more than 30 Myr (and still yet to reach a steady
301 state). The river-channel reversal rate decreases exponentially over time (Fig. 4D).
302 Moreover, the uplift rate facilitates the river-channel reversal. A higher uplift rate
303 results in a faster reversal rate and thus a longer reversal distance (Figs. 3C-D).

304 **2.4 Effects of erosional coefficient**

305 Lithology and climate can also affect the migration of drainage divides (e.g.,
306 Willett et al., 2001, 2014; Zondervan et al., 2020; Zhou et al., 2022a). Their effects are
307 implemented in the rock erosion coefficient in our models. A smaller erosion
308 coefficient means a stronger lithological unit or lower precipitation. Therefore, we
309 designed one group of models to examine the influence of the erosional coefficient
310 (Figs. 4E-F; Supplementary Fig. S3). The erosional coefficient is spatially uniform

311 and varies between 10^{-6} /year and 10^{-5} /year for different models, which is comparable
 312 to the values in the natural landscapes (e.g., [Stock and Montgomery, 1999](#)).

313 In this series of models, our results show that a low initial rock erosion
 314 coefficient is beneficial for the migration of the newly-formed drainage divide ([Figs.](#)
 315 [4E-F](#)). A minor rock coefficient induces a lower erosion rate, which results in a flat,
 316 plateau-like surface across the south-flowing rivers in the early stage ([Supplementary](#)
 317 [Fig. S3](#)). This allows the captor rivers to drive the drainage divide to migrate rapidly
 318 southward, which results in a faster reversal rate ([Fig. 4F](#)). In contrast, a higher
 319 erosion coefficient accelerates river erosion but hinders divide migration and
 320 river-channel reversal.



322 **Fig. 4** The change of river-channel reversal distance and reversal rate over time in the models
323 with different captured areas (A, B), uplift rates (C, D), and erosional efficiencies (E, F). The
324 results show that the reversal rate exponentially decreases with time. The higher uplift rate,
325 larger captured area, and lower erosional coefficient can lead to a faster reversal rate and thus
326 longer reversal distance.

327 **4 Application to natural landscapes**

328 As above numerical modeling demonstrates, after a capture event, the
329 newly-formed drainage divide between the reversal river and the beheaded river
330 would migrate from the capture point towards the beheaded-river side until it reaches
331 equilibrium or even undergoes an overturn. Therefore, in the case study, the stability
332 and the location of the newly-formed drainage divides play a crucial role in revealing
333 the river network reorganization process. Here, we evaluated the stability of the
334 Dadu-Anning and Yarlung-Yigong drainage divides, respectively. With that, we
335 predicate the future steady location of the Dadu-Anning drainage divide.

336 **4.1 Dynamic Dadu-Anning drainage divide**

337 Drainage-divide migration is essentially driven by the cross-divide difference in
338 erosion rate (Willett et al., 2014; Forte and Whipple, 2018; He et al., 2021; Zhou et al.,
339 2022a). Because the normalized channel steepness (k_{sn}) is positively and
340 monotonically correlated with erosion rate (Kirby and Whipple, 2012), the
341 comparisons on the k_{sn} value across the drainage divide have been used to evaluate the
342 drainage-divide stability, assuming similar lithology and precipitation (Willett et al.,
343 2014; Forte and Whipple, 2018; Chen et al., 2021). In particular, the k_{sn} value can be
344 visualized by the slope of the χ -plots. Therefore, when comparing the top-most k_{sn}
345 value (linear or quasi-linear χ -plots), a greater value (i.e., a steeper slope of χ -plot)

346 would force the drainage divide to migrate towards the other side (Zhou et al., 2022b).

347 We compared the cross-divide differences in topographic features, k_{sn} , and χ by

348 the satellite imagery and χ map (Fig. 5). The Dadu drainage has steeper channels,

349 higher k_{sn} , and lower χ values than those in the Anning drainage (Figs. 5A, B, D).

350 Here, we show three paired tributaries through similar lithologies to compute the

351 χ -plots. Among them, a pair of rivers close to the broad valley is characterized by a

352 signature of drainage area gain by tributaries shift in the χ -plot (Fig. 5C) (Willett et al.,

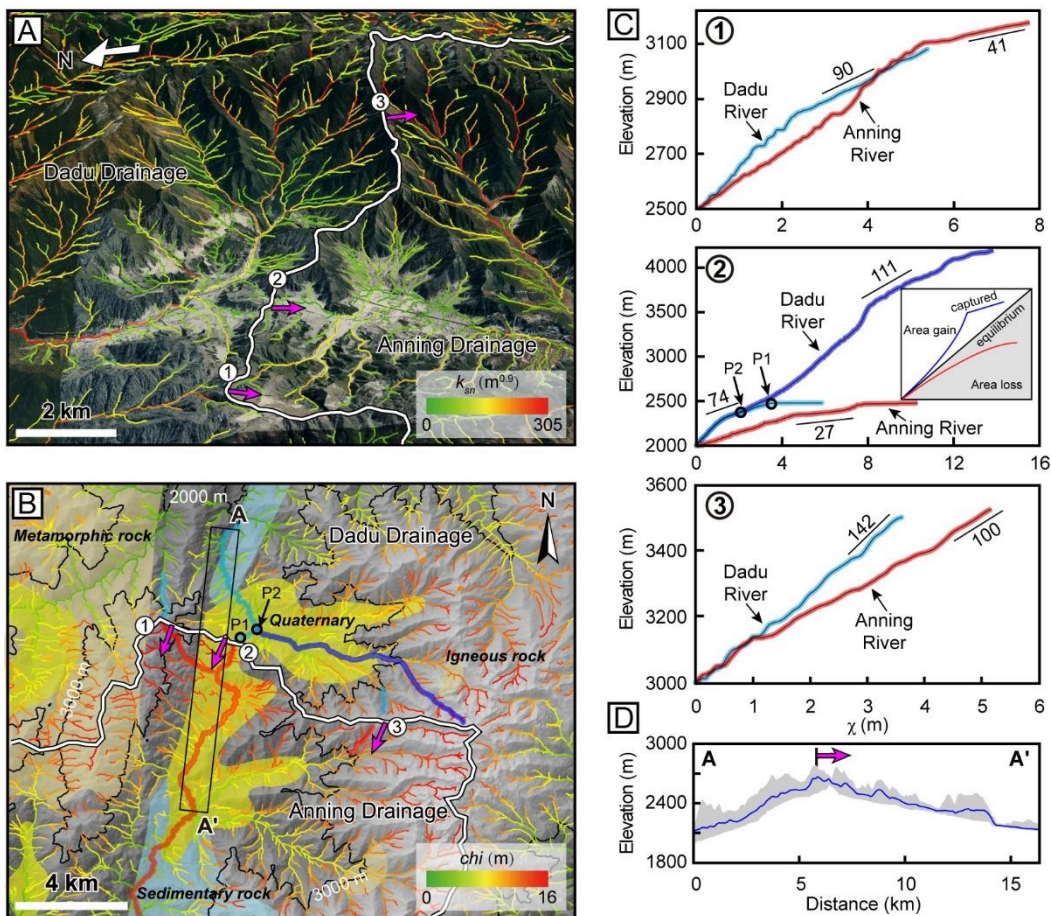
353 2014; Beeson et al., 2017). For other rivers, the upper reaches of the Dadu River have

354 higher k_{sn} values (greater slopes) than those of the Anning River (Fig. 5C), indicating

355 that the drainage divide is migrating southward. In summary, the above different

356 methods show consistent results, where the Dadu-Anning drainage divide is moving

357 south.



358

359 **Fig. 5** Perspective views and χ map of channels for part of the Dadu-Anning drainage divides.
 360 The location is shown in **Fig. 2B**. (A) Perspective views of channels mapped with k_{sn} . The k_{sn}
 361 values in the Dadu drainage are generally larger than those in the Anning drainage. (B) Map
 362 of χ and geology. Arrows show the divide migration directions. P₁ and P₂ are the capture
 363 points. (C) χ -plots for three paired rivers across the divide. Numbers in the χ -plots are the
 364 average k_{sn} values. Rivers in red are the victims and those in blue are the aggressors. The
 365 results show that the Dadu-Anning divide is moving south. The reference drainage area is 10⁵
 366 m². (D) Swath profile A-A' of topography across the divide. Location of the swath is marked
 367 by the black rectangle in panel (B).

368 4.2 Future stable location of the Dadu-Anning drainage divide

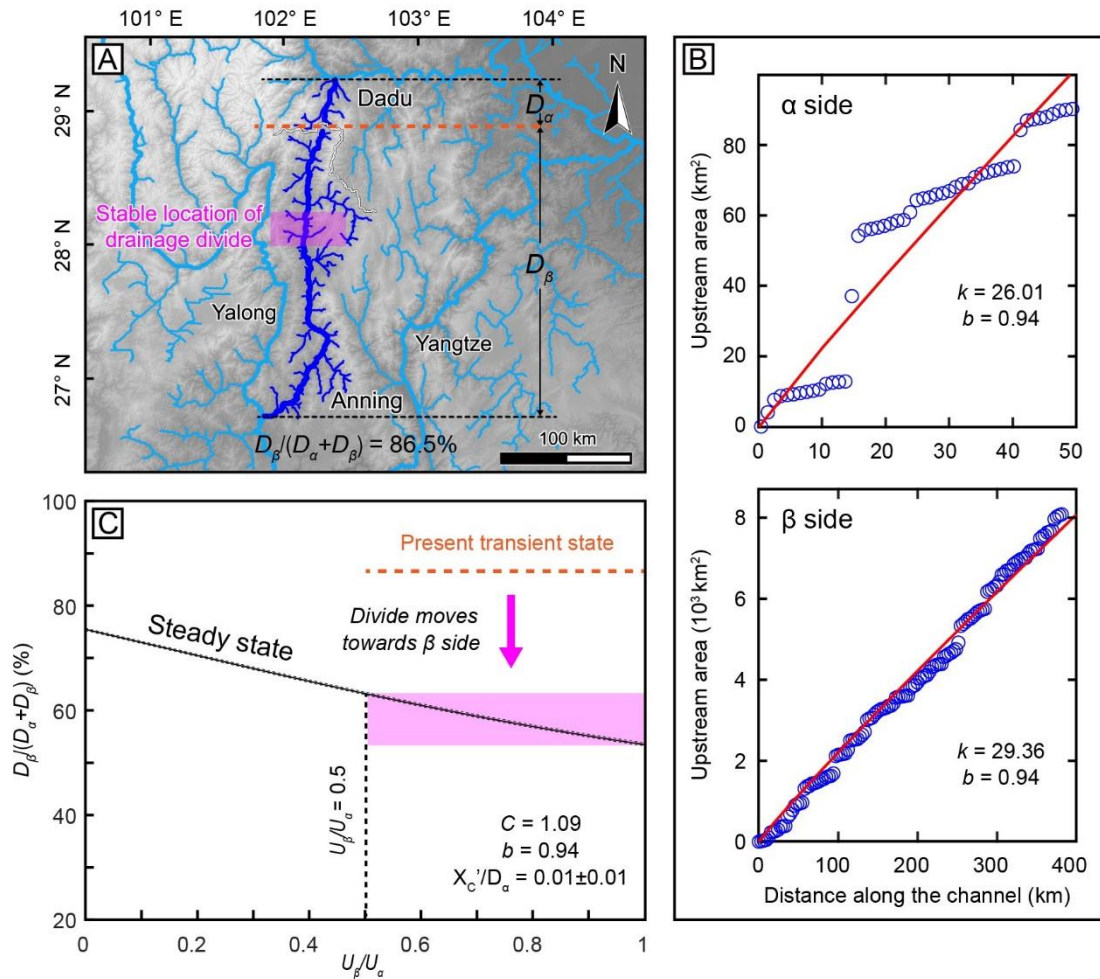
369 To predicate the future steady location of the drainage divide, we calculated the
 370 cross-divide contrast index (C) (Zhou et al., 2022a). It amalgamates the across-divide
 371 differences in lithology, precipitation, channel height, and drainage-basin morphology
 372 by a quantitative theoretical relationship between the erosion coefficient (K), channel
 373 height (H), tortuosity coefficient (T), Hack's coefficient and exponent (k and b), area
 374 exponent (m), and slope exponent (n).

$$375 \quad C = \left(\frac{K_{\beta}}{K_{\alpha}}\right)^{\frac{1}{n}} \left(\frac{H_{\beta}}{H_{\alpha}}\right) \left(\frac{T_{\beta}}{T_{\alpha}}\right)^{\frac{mb}{n}-1} \left(\frac{k_{\beta}}{k_{\alpha}}\right)^{\frac{m}{n}} \quad (1)$$

376 where subscripts α and β represent the two sides of the drainage divide. In this study,
 377 α is the northern side, and β is the southern side.

378 A pair of typical rivers close to the wind gap was selected (**Fig. 6A**). They flow
 379 into the main trunk of the Dadu and Yangtze Rivers, respectively. We measured the H
 380 and T at each side of the divide in ArcGIS software and determined the Hack's
 381 coefficient (k_{α} and k_{β}) and exponent (b) by fitting the drainage area and channel
 382 length (**Fig. 6B**) (Hack, 1957; Zhou et al., 2022a). Then, we calculated the C value
 383 combined with a uniform erosion coefficient ($K_{\beta}/K_{\alpha}=1$). The detailed results are

384 shown in Supplementary Table S1. Accordingly, we plotted the relationship diagram
 385 between the normalized drainage divide location ($D_\beta/(D_\alpha + D_\beta)$) and uplift rate ratio
 386 (U_β/U_α) (Fig. 6C). With a wide range of the U_β/U_α (0.5–1), the $D_\beta/(D_\alpha + D_\beta)$ value is
 387 determined as 63.2%–53.5%. Based on the present normalized location of the
 388 Dadu-Anning divide (~86.5%), we predict that the drainage divide would continue to
 389 migrate southward for ~65–92 km. It is worth noting that there may be errors in this
 390 value due to the inhomogeneous lithology (Supplementary Fig. S4) along the river
 391 channel.
 392



393
 394 **Fig. 6** Prediction for the steady location of the Dadu-Anning drainage divide. (A) Topography
 395 and drainage system. River segments highlighted in dark blue are measured and analyzed.

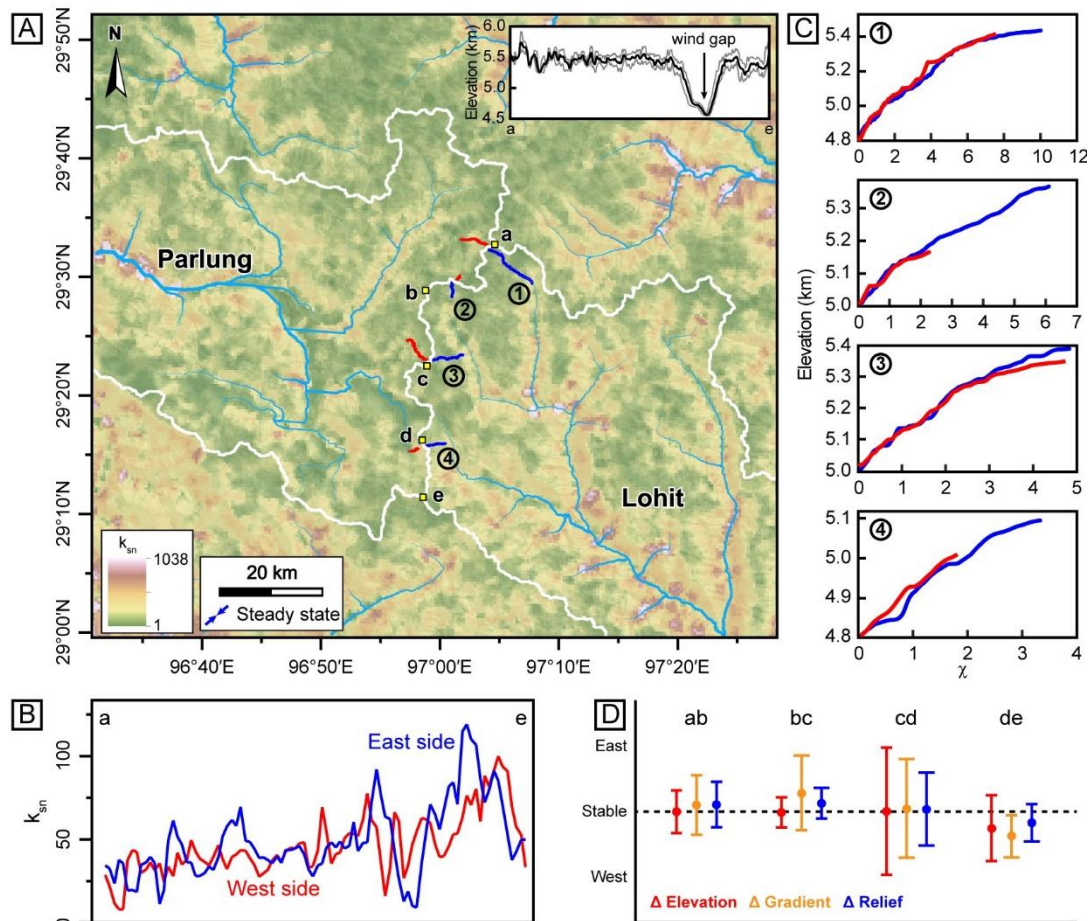
396 The burgundy area is the predicted steady location. (B) The Hack's coefficient and exponent
397 (k and b). (C) The relationship diagram between the normalized drainage divide location
398 ($D_\beta / (D_\alpha + D_\beta)$) and uplift rate ratio (U_β/U_α).

399 4.3 Stable Yarlung-Yigong drainage divide

400 To analyze the stability of the Parlung-Lohit drainage divide, we first compared
401 the difference in k_{sn} value across the divide (Willett et al., 2014; Scherler and
402 Schwanghart, 2020). Fig. 7A is the k_{sn} distribution pattern yield by the ArcGIS
403 software. Along a 500-meter-wide swath, the k_{sn} values are comparable between two
404 sides of the drainage divide (Fig. 7B). We also measured the top-most k_{sn} value of
405 four paired rivers across the drainage divide. These rivers are distributed in four
406 sections of the Parlung-Lohit drainage divide (the ab, bc, cd, and de sections),
407 respectively. The χ -plot pairs show near-parallel profiles and thus approximately equal
408 k_{sn} values (Fig. 7C). Therefore, the results show that the Parlung-Lohit drainage
409 divide is stable.

410 In addition, we adopted the Gilbert metrics method (Forte and Whipple, 2018) to
411 analyze the four segments along the drainage divide. The Gilbert metrics incorporate
412 the cross-divide differences in mean headwater local relief, mean headwater hillslope
413 gradient, and channel elevation at a reference drainage area (Whipple et al., 2017;
414 Forte and Whipple, 2018). The drainage divide will migrate towards the side with a
415 lower slope, lower relief, or higher elevation in an asymmetrical mountain. In this
416 study, we used a reference drainage area of 10^5 m^2 to calculate the Gilbert metrics.
417 According to the standardized analysis of drainage migration direction (Fig. 7D), four
418 segments show that the current divide is at a stable state, which is consistent with the
419 results from the χ -plots.

420



421

422 **Fig. 7** (A) The k_{sn} map of the Yigong and Parlung drainages. See Fig. 2C for location. Insert
 423 figure is an elevation profile along the drainage divide (a-e), where the black arrows indicate
 424 the locations of the wind gaps. (B) Comparison of the k_{sn} values between the two sides of the
 425 Yigong-Parlung drainage divide along a 500-meter-wide swath. (C) χ -plots for four paired
 426 rivers across the divide. (D) Standardized delta plot for the four segments along the
 427 Yigong-Parlung drainage divide. The results are calculated by the DivideTools in
 428 TopoToolbox (Schwanghart and Scherler, 2014; Forte and Whipple, 2019). The different
 429 methods above show consistent results, where the Yigong-Parlung divide is steady.

430 5 Discussion

431 5.1 Effects of different parameters on divide migration following a capture event

432 A capture event can significantly adjust the river network topology, and thus

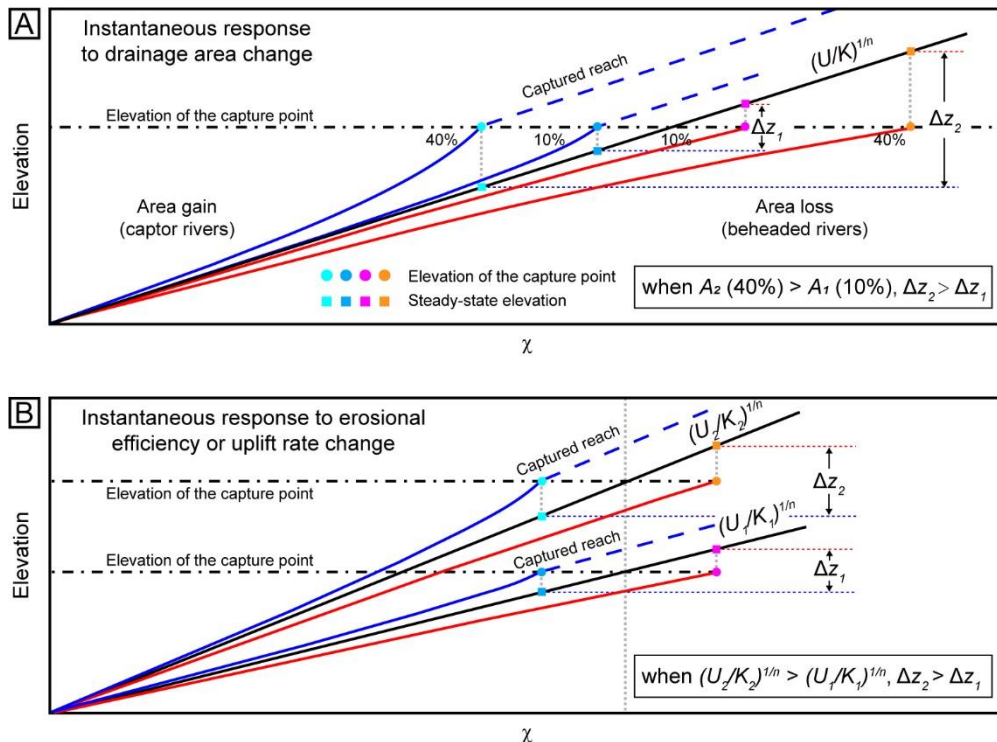
433 cause an abrupt change of steady-state elevations along river channels. Willett et al.
434 (2014) suggested that the drainage divide will migrate towards the river basin with
435 higher steady-state elevation at the channel head. In this way, the drainage-divide
436 migration following a river capture event is closely related to the cross-divide
437 difference in steady-state elevation at the channel heads.

438 Based on the quantitative relationships (Eqs. 5 and 6) of the steady-state
439 elevation, we analyzed the effects of capture area, uplift rate, and erosional coefficient
440 on drainage-divide migration. A sudden adjustment in drainage area instantaneously
441 changes χ but not riverbed elevation (Willett et al., 2014; Whipple et al., 2017). In
442 general, the channel head of the captor river has a lower steady-state elevation than
443 that at the future capture point, which drives the divide migration and eventually leads
444 to the capture event. However, for brevity, we assume that the channel head of the
445 captor river has a similar steady-state elevation to that at the future capture point
446 before the capture event. That is to say, the pre-existing cross-divide difference of
447 steady-state elevation before the capture event was not taken into account. After a
448 capture event, the beheaded river loses lots of upstream areas, which causes the
449 increase of χ and then yields a higher steady-state elevation (Fig. 8A) (Willett et al.,
450 2014). Similarly, the decrease in χ with area gain for captor rivers leads to a lower
451 steady-state elevation. Therefore, the capture event will substantially increase the
452 contrast of the steady-state elevation across the newly-formed drainage divide. A
453 larger captured area can theoretically expand this contrast (Fig. 8A). The numerical
454 modeling results reveal that a larger captured area will drive faster drainage-divide

455 migration when other conditions are the same (Figs. 4A-B).

456 In the case of increasing uplift rate or decreasing erosional coefficient (with other
 457 conditions being unchanged), the captor and beheaded rivers experience a uniform
 458 increase in riverbed elevation, and the steady state profile ($E = U$) becomes steeper
 459 accordingly (Fig. 8B). A capture event (with the same captured area) will increase the
 460 cross-divide difference in the steady-state elevation at the channel heads (Fig. 8B).
 461 Higher uplift rate or lower erosional coefficient will drive the higher cross-divide
 462 difference in the steady-state elevation at the channel heads, and further enhance the
 463 rate of drainage-divide migration, which is consistent with the result in the numerical
 464 modeling (Figs. 4C-F).

465



466

467 **Fig. 8** (A) Schematic illustration of river profile response to drainage area change. A capture

468 event will decrease the steady-state elevation for captor rivers gaining upstream area and

469 increase the steady-state elevation for the beheaded rivers losing upstream area. A larger

470 captured area can expand this contrast, and accelerate the divide migration. (B) Schematic
471 illustration of river profile response to uplift rate and erosion coefficient change. Increasing
472 the uplift rate or decreasing the erosional coefficient can increase a cross-divide steady-state
473 elevation contrast. Δz represents the cross-divide difference in steady-state channel-head
474 elevation.

475

476 In summary, the larger captured area, higher uplift rate, or lower erosional
477 coefficient can cause higher cross-divide differences in steady-state elevation of the
478 channel heads, which facilitates the migration of the newly-formed drainage divide
479 following a capture event.

480 **5.2 The timescale of the Dadu-Anning drainage divide achieving a steady state**

481 The modern Dadu and Anning Rivers have experienced an Early Pleistocene
482 (~2.4 Ma) capture event (Yang et al., 2020), where the upper course of the original
483 southward-flowing paleo-Dadu-Anning River was captured by an east-flowing
484 paleo-Dadu River (Fig. 2B). The newly-formed Dadu-Anning drainage divide has
485 migrated southward for ~40 km from the capture point (Fig. 2B). The result
486 corresponds to a mean river-channel reversal rate of ~16.7 mm/yr from the moment
487 of the capture event to present.

488 Our results show that the Dadu-Anning drainage divide is moving south at
489 present, and would further migrate ~65–92 km southward to reach a steady state (Fig.
490 6). It implies that the present Dadu-Anning drainage divide has only migrated less
491 than half of the total migration (from the capture point to the final steady state of the
492 drainage divide). Meanwhile, our numerical modeling indicates that the reversal rate
493 rapidly decreases to half of the original value after ~2–3 Myr (Fig. 4). If, thereafter,

494 the channel reversal rate decreases to ~8.4 mm/yr, the Dadu-Anning divide would
495 take another ~11–8 Ma to reach a steady state. Taking into account that the reversal
496 rate further decreases with time in the future (Fig. 4), this timescale of the
497 drainage-divide migration to achieve an equilibrium will be significantly extended.
498 Therefore, we conclude that the Dadu-Anning drainage divide would reach a steady
499 state in tens of millions of years, which is consistent with that in the numerical
500 modeling in this study (Figs. 3, 4) and those in previous studies (Shelef and Goren,
501 2021; Ye et al., 2022).

502 **5.3 Constraints on the timing of the Yarlung-Yigong capture event**

503 The current Parlung River has reversed its direction and flows northwest for
504 more than 200 km. However, the timing of this capture event is a subject of
505 controversy. One proposed explanation is that the paleo-Yarlung-Parlung-Irrawaddy
506 River was captured by the Siang River, leading to the reversal of the Parlung River
507 (Clark et al., 2004). This capture event was constrained at ~10 Ma (Brookfield, 1998;
508 Robinson et al., 2014) or prior to ~4 Ma (Zeitler et al., 2001; Clark et al., 2004).
509 Alternatively, recent studies have argued that the headward cutting
510 Yarlung-Siang-Brahmaputra captured the Parlung River in the Quaternary, as
511 indicated by thermochronological data (Seward and Burg, 2008; Zeitler et al., 2014;
512 King et al., 2016; Yang et al., 2021) and provenance analysis (Lang and Huntington,
513 2014; Govin et al., 2018).

514 Our observations, based on the stability analysis and numerical modeling,
515 provide a new perspective on this debate. We find that the Parlung-Lohit drainage
516 divide is stable at present (Fig. 7), which implies that it has migrated ~200 km from
517 the capture point towards the southeast and reached a steady state. According to the

518 modeling results in this study (Fig. 4) and those in previous studies (Willett et al.,
519 2014; Beeson et al., 2017; Whipple et al., 2017; Shelef and Goren, 2021), the
520 river-channel reversal process could continue for tens of million years. Therefore, a
521 Quaternary capture event would not be sufficient for a newly-formed drainage divide
522 to achieve an equilibrium position. This idea can also be supported by the case of the
523 Dadu-Anning capture, where the divide only migrated ~40 km to the south within
524 ~2.4 Ma (Yang et al., 2020) and is currently moving south with a largely decreased
525 migration rate but a longer remaining distance (~65–92 km) (Fig. 5). Furthermore, the
526 area of the Yigong Drainage (~13000 km²) captured by Yarlung-Brahmaputra or the
527 Siang Rivers is much smaller than the captured area (~64000 km²) by the paleo-Dadu
528 River, making it even more unlikely that the time of the Yarlung-Yigong capture event
529 is earlier than that of the Dadu-Anning capture event. Therefore, the results in this
530 study support that the Yarlung-Yigong capture event occurred in the early-middle
531 Cenozoic.

532 In the Namche Barwa syntaxis, bedrock and detrital thermochronology data
533 revealed an acceleration of exhumation rates along the lower reaches of the Yigong
534 and Parlung Rivers in the past 1–2 Ma (Seward and Burg, 2008; King et al., 2016;
535 Bracciali et al., 2016; Yang et al., 2018, 2021; Govin et al., 2020). This rapid
536 exhumation was suggested as a signal for the capture event of the Parlung River.
537 However, our results tend to favor an early formation of the current Yarlung River
538 pattern, rather than the hypothesis of Quaternary capture. It implies that the late
539 Cenozoic increased exhumation rate is not driven by the capture event. In this case,
540 the increased exhumation in the northern part may be attributed to a northward
541 expansion of the syntaxis (Seward and Burg, 2008; Wang et al., 2014; King et al.,
542 2016; Yang et al., 2018). In addition, spatiotemporal variations of precipitation may

543 play a role in the rapid exhumation. The strengthened precipitation in the lower
544 reaches of the Yarlung River can reduce the elevation of the riverbed, which can
545 accelerate the exhumation in Namche Barwa syntaxis (Zeitler et al., 2001; Yu et al.,
546 2011).

547 This study demonstrates the process of drainage-divide migration following a
548 river capture event, which helps to understand the evolution of rivers and offers an
549 opportunity to constrain the time of capture events from a new perspective. However,
550 there are still some limitations in this study. Our modeling does not account for the
551 presence of unconsolidated sediments, which are commonly associated with river
552 capture events (Clark et al., 2004; Zeng and Tan, 2023). This may result in an
553 underestimation of the simulated reversal rate. In addition, the tributaries and their
554 avulsions on drainage-divide migration can play a critical role in the reversal rate and
555 extent (Shelef and Goren, 2021), but are not considered in our models. How these two
556 factors influence the migration of the newly-formed drainage divide following a river
557 capture event, however, is beyond the scope of this study, and deserves rigorous
558 analysis in future studies.

559 **6 Conclusions**

560 (1) Numerical modeling results show that the newly-formed drainage divide
561 following a river capture event will migrate lasting for tens of millions of years, with
562 the migration rate decreasing exponentially over time. A larger captured area, higher
563 uplift rate, or lower erosional coefficient can increase cross-divide steady-state
564 elevation contrast, and further enhance the rate of drainage-divide migration.

565 (2) The present Dadu-Anning divide is moving south, which would last for tens
566 of millions of years and further migrate ~65–92 km southward to reach a steady state.

567 (3) The Parlung River has reversed its flow direction for over 200 km after the
568 Yarlung-Yigong capture event, and the river network has reached a new steady state.
569 Our findings support an early formation of the modern Yarlung River, rather than the
570 hypothesis of the Quaternary capture event of the Parlung River. This implies that the
571 late Cenozoic increased exhumation rate was not driven by the Yarlung-Yigong
572 capture event.

573 **Acknowledgments**

574 This study is supported by the Fundamental Research Funds for the State Key Laboratory of
575 Earthquake Dynamics (LED2022A04 and LED2021A02), the CAS Pioneer Hundred Talents
576 Program (E2K2010010), the National Natural Science Foundation of China (42202249).
577

578 **Data Availability Statement**

579 The topography data is from <https://search.asf.alaska.edu/>. The precipitation data are
580 downloaded from <http://worldclim.org>. Procedures to perform the calculations are implemented
581 through the Topographic Analysis Kit (Forte and Whipple, 2019) and DivideTools (Forte and
582 Whipple, 2018) based on TopoToolbox (Schwanghart and Scherler, 2014).
583

584 **References**

585 Beeson, H. W., Mccoy, S. W., & Keen-Zebert, A. (2017). Geometric disequilibrium of river basins
586 produces long-lived transient landscapes. *Earth and Planetary Science Letters*, 475, 34–43.
587 <https://doi.org/10.1016/j.epsl.2017.07.010>

588 Bishop, P. (1995). Drainage rearrangement by river capture, beheading and diversion. *Progress in*
589 *Physical Geography*, 19, 449–473. <https://doi.org/10.1177/030913339501900402>

590 Bracciali, L., Najman, Y., Parrish, R. R., Akhter, S. H. & Millar, I. (2015). The Brahmaputra tale
591 of tectonics and erosion: Early Miocene river capture in the Eastern Himalaya. *Earth and*
592 *Planetary Science Letters*, 415, 25–37. <https://doi.org/10.1016/j.epsl.2015.01.022>

593 Bracciali, L., Parrish, R. R., Najman, Y., Smye, A., Carter, A., & Wijbrans, J. R. (2016).
594 Plio-Pleistocene exhumation of the eastern Himalayan syntaxis and its domal ‘pop-up’.
595 *Earth-science Reviews*, 160, 350–385. <https://doi.org/10.1016/j.earscirev.2016.07.010>

596 Braun, J. (2017). A review of numerical modeling studies of passive margin escarpments leading
597 to a new analytical expression for the rate of escarpment migration velocity. *Gondwana*
598 *Research*, 53, 209–224. <https://doi.org/10.1016/j.gr.2017.04.012>

599 Brocard, G., Teyssier, C., Dunlap, W. J., Authemayou, C., Simon-Labric, T., Cacao-Chiquín, E. N.,
600 et al. (2011). Reorganization of a deeply incised drainage: Role of deformation,
601 sedimentation and groundwater flow. *Basin Research*, 23(6), 631–651.
602 <https://doi.org/10.1111/j.1365-2117.2011.00510.x>

603 Brookfield, M. (1998). The evolution of the great river systems of southern Asia during the
604 Cenozoic India-Asia collision: rivers draining southwards. *Geomorphology*, 22, 285–312.
605 [https://doi.org/10.1016/S0169-555X\(97\)00082-2](https://doi.org/10.1016/S0169-555X(97)00082-2)

606 Burchfiel, B. C., Clark, M. K., Wang, E., Chen, Z., Liu, Y., & Pan, G. (2000). Tectonic framework
607 of the Namche Barwa region, eastern Himalayan syntaxis, SE Tibet. *Geological Society of*
608 *America Special Paper*, 32(7), A–33.

609 Campforts, B., Schwanghart, W., & Govers, G. (2017). Accurate simulation of transient landscape
610 evolution by eliminating numerical diffusion: the TTLEM 1.0 model. *Earth Surface*
611 *Dynamics*, 5(1), 47–66. <https://doi.org/10.5194/esurf-5-47-2017>

612 Chen, C., Willett, S. D., Christl, M., & Shyu, J. B. H. (2021). Drainage basin dynamics during the
613 transition from early to mature orogeny in Southern Taiwan. *Earth and Planetary Science*
614 *Letters*, 562, 116874. <https://doi.org/10.1016/j.epsl.2021.116874>

615 Chen, Y., Yan, M., Fang, X., Song, C., Zhang, W., Zan, J., et al. (2017). Detrital zircon U-Pb
616 geochronological and sedimentological study of the Simao Basin, Yunnan: implications for

617 the Early Cenozoic evolution of the Red River. *Earth and Planetary Science Letters*, 476, 22–
618 33. <https://doi.org/10.1016/j.epsl.2017.07.025>

619 Cina, S. E., An, Y., Grove, M., Dubey, C. S., Shukla, D. P., Lovera, O. M., et al. (2009). Gangdese
620 arc detritus within the eastern Himalayan Neogene foreland basin: implications for the
621 Neogene evolution of the Yalu-Brahmaputra River system. *Earth and Planetary Science
622 Letters*, 285(1–2), 150–162. <https://doi.org/10.1016/j.epsl.2009.06.005>

623 Clark, M., Schoenbohm, L. M., Royden, L. H., Whipple, K. X., Burchfiel, B. C., Zhang, X., et al.
624 (2004). Surface uplift, tectonics, and erosion of eastern Tibet from large-scale drainage
625 patterns. *Tectonics*, 23(1), TC1006. <https://doi.org/10.1029/2002TC001402>

626 Clift, P.D., Blusztajn, J., & Anh Duc, N. (2006). Large-scale drainage capture and surface uplift in
627 eastern Tibet-SW China before 24 Ma inferred from sediments of the Hanoi Basin, Vietnam.
628 *Geophysical Research Letters*, 33, 19. <http://dx.doi.org/10.1029/2006GL027772>, L19403.

629 Fan, N. N., Chu, Z., Jiang, L., Hassan, M. A., Lamb, M. P., & Liu, X. (2018). Abrupt drainage
630 basin reorganization following a Pleistocene river capture. *Nature Communication*, 9, 1–6.
631 <https://doi.org/10.1038/s41467-018-06238-6>

632 Fan, N. N., Kong, P., Robl, J. C., Zhou, H. W., Wang, X. Y., Jin, Z. D., et al. (2021). Timing of
633 river capture in major Yangtze River tributaries: Insights from sediment provenance and
634 morphometric indices. *Geomorphology*, 392, 107915.
635 <https://doi.org/10.1016/j.geomorph.2021.107915>

636 Fan, N. N., Wu, B. & Liu, L. (2010). River avulsion by earthquake and the transition of ancient
637 Shu Civilization. *Journal of Mountain Science*, 28, 453–462. (in Chinese with an English
638 abstract).

639 Forte, A. M., & Whipple, K. X. (2018). Criteria and tools for determining drainage divide stability.
640 *Earth and Planetary Science Letters*, 493, 102–117. <https://doi.org/10.1016/j.epsl.2018.04.026>

641 Forte, A. M., & Whipple, K. X. (2019). Short communication: The Topographic Analysis Kit
642 (TAK) for TopoToolbox. *Earth Surface Dynamics*, 7, 87–95.

643 Goren, L., Fox, M., & Willett, S. D. (2014). Tectonics from fluvial topography using formal linear
644 inversion; theory and applications to the Inyo Mountains, California. *Journal of Geophysical
645 Research: Earth Surface*, 119, 1651–1681. <https://doi.org/10.1002/2014JF003079>

646 Gourbet, L., Leloup, P. H., Paquette, J.L., Sorrel, P., Maheo, G., Wang, G., et al. (2017).
647 Reappraisal of the Jianchuan Cenozoic basin stratigraphy and its implications on the SE
648 Tibetan plateau evolution. *Tectonophysics*, 700–701, 162–179.
649 <https://doi.org/10.1016/j.tecto.2017.02.007>

650 Govin, G., Najman, Y., Copley, A., Millar, I., van der Beek, P., Huyghe, P., et al. (2020). Early
651 onset and late acceleration of rapid exhumation in the Namche Barwa syntaxis, eastern
652 Himalaya. *Geology*, 48(12), 1139–1143. <https://doi.org/10.1130/G47720.1>

653 Govin, G., Najman, Y., Dupont-Nivet, G., Millar, I., van der Beek, P., Huyghe, P., et al. (2018).
654 The tectonics and paleo-drainage of the easternmost Himalaya (Arunachal Pradesh, India)
655 recorded in the Siwalik rocks of the foreland basin. *American Journal of Science*, 318, 764–
656 798. <https://doi.org/10.2475/07.2018.02>

657 Hack, J. T. (1957). Studies of longitudinal stream profiles in Virginia and Maryland. In: U.S.
658 Geological Survey Professional Paper, pp. 45–97

659 Harel, E., Goren, L., Shelef, E., & Ginat, H. (2019). Drainage reversal toward cliffs induced by
660 lateral lithologic differences. *Geology*, 47, 928–932. <https://doi.org/10.1130/G46353.1>

661 He, C. Q., Yang, C. J., Turowski, J. M., Rao, G., Roda-Boluda, D. C., & Yuan, X. P. (2021).
662 Constraining tectonic uplift and advection from the main drainage divide of a mountain belt.
663 *Nature Communication*, 12(1), 544. <https://doi.org/10.1038/s41467-020-20748-2>

664 He, C., Rao, G., Yang, R., Hu, J., Yao, Q., & Yang, C. J. (2019). Divide migration in response to
665 asymmetric uplift: Insights from the Wula Shan horst, North China. *Geomorphology*, 339,
666 44–57. <https://doi.org/10.1016/j.geomorph.2019.04.024>.

667 Hoorn, C., Wesselingh, F. P., ter Steege, H., Bermudez, M. A., Mora, A., Sevink, J., et al. (2010).
668 Amazonia through time: Andean uplift, climate change, landscape evolution, and biodiversity.
669 *Science*, 330, 927–931. <https://doi.org/10.1126/science.1194585>

670 Howard, A.D., & Kerby, G., 1983. Channel changes in badlands. *Geological Society of America*
671 *Bulletin*, 94(6), 739–752. [https://doi.org/10.1130/0016-7606\(1983\)94<739:CCIB>2.0.CO;2](https://doi.org/10.1130/0016-7606(1983)94<739:CCIB>2.0.CO;2)

672 King, G. E., Herman, F., & Guralnik, B. (2016). Northward migration of the eastern Himalayan
673 syntaxis revealed by OSL thermochronometry. *Science*, 353, 800–804.
674 <https://doi.org/10.1126/science.aaf2637>

675 Kirby, E., & Whipple, K. (2001). Quantifying differential rock-uplift rates via stream profile
676 analysis. *Geology*, 29(5), 415–418.
677 [https://doi.org/10.1130/0091-7613\(2001\)029<0415:QDRURV>2.0.CO;2](https://doi.org/10.1130/0091-7613(2001)029<0415:QDRURV>2.0.CO;2).

678 Kirby, E., & Whipple, K. X. (2012). Expression of active tectonics in erosional landscapes.
679 *Journal of Structural Geology*, 44, 54–75. <https://doi.org/10.1016/j.jsg.2012.07.009>

680 Lang, K. A., & Huntington, K. W. (2014). Antecedence of the Yarlung-Siang-Brahmaputra River,
681 eastern Himalaya. *Earth and Planetary Science Letters*, 397, 145–158.
682 <https://doi.org/10.1016/j.epsl.2014.04.026>

683 Lave, J. (2015). Landscape inversion by stream piracy. *Nature*, 520, 442–444.

684 Mitchell, N. A., & Yanites, B. J. (2019). Spatially variable increase in rock uplift in the northern
685 US Cordillera recorded in the distribution of river knickpoints and incision depths. *Journal of*
686 *Geophysical Research: Earth Surface*, 124(5), 1238–1260.
687 <https://doi.org/10.1029/2018JF004880>

688 Morisawa, M. (1989). Rivers and valleys of Pennsylvania, revisited. *Geomorphology*, 2, 1–22.

689 Perron, J.T., & Royden, L. (2013). An integral approach to bedrock river profile analysis. *Earth*
690 *Surface Processes and Landforms*, 38 (6), 570–576. <https://doi.org/10.1002/esp.3302>.

691 Prince, P. S., Spotila, J. A. & Henika, W. S. (2011). Stream capture as driver of transient landscape
692 evolution in a tectonically quiescent setting. *Geology*, 39, 823–826.
693 <https://doi.org/10.1130/G32008.1>

694 Robinson, R. A., Brezina, C. A., Parrish, R. R., Horstwood, M. S. A., Oo, N. W., Bird, M. I., et al.
695 (2014). Large rivers and orogens: The evolution of the Yarlung Tsangpo-Irrawaddy system
696 and the eastern Himalayan syntaxis. *Gondwana Research*, 26, 112–121.
697 <https://doi.org/10.1016/j.gr.2013.07.002>

698 Scherler, D., & Schwanghart, W. (2020). Drainage divide networks – part 2: Response to
699 perturbations. *Earth Surface Dynamics*, 8 (2), 261–274.
700 <https://doi.org/10.5194/esurf-8-261-2020>

701 Schwanghart, W., & Scherler, D. (2014). TopoToolbox 2–MATLAB-based software for
702 topographic analysis and modeling in Earth surface sciences. *Earth Surface Dynamics*, 2, 1–7.
703 <https://doi.org/10.5194/esurf-2-1-2014>

704 Seward, D., & Burg, J. P. (2008). Growth of the Namche Barwa Syntaxis and associated evolution
705 of the Tsangpo Gorge; constraints from structural and thermochronological data.
706 *Tectonophysics*, 451, 282–289. <https://doi.org/10.1016/j.tecto.2007.11.057>

707 Shelef, E., & Goren, L. (2021). The rate and extent of wind-gap migration regulated by tributary
708 confluences and avulsions. *Earth Surface Dynamics*, 9(4), 687–700.
709 <https://doi.org/10.5194/esurf-2021-11>

710 Shi, F., Tan, X., Zhou, C., & Liu, Y. (2021). Impact of asymmetric uplift on mountain asymmetry:
711 Analytical solution, numerical modeling, and natural examples. *Geomorphology*, 389,
712 107862. <https://doi.org/10.1016/j.geomorph.2021.107862>

713 Stock, J. D., & Montgomery, D. R. (1999). Geologic constraints on bedrock river incision using
714 the stream power law. *Journal of Geophysical Research: Solid Earth*, 104, 4983–4993.
715 <https://doi.org/10.1029/98JB02139>

716 Stokes, M. F., Goldberg, S. L., & Perron, J. T. (2018). Ongoing river capture in the Amazon,
717 *Geophysical Research Letters*, 45, 5545–5552, <https://doi.org/10.1029/2018GL078129>

718 Wang, P., Scherler, D., Liu-Zeng, J., Mey, J., Avouac, J.P., Zhang, Y., et al. (2014). Tectonic
719 control of Yarlung Tsangpo Gorge revealed by a buried canyon in Southern Tibet. *Science*,
720 346, 978–981. <https://doi.org/10.1126/science.1259041>

721 Wei, H. H., Wang, E. C., Wu, G. L. & Meng, K. (2016). No sedimentary records indicating
722 southerly flow of the paleo-Upper Yangtze River from the First Bend in southeastern Tibet.
723 *Gondwana Research*, 32, 93–104. <https://doi.org/10.1016/j.gr.2015.02.006>

724 Whipple, K. X. (2001). Fluvial landscape response time: How plausible is steady-state
725 denudation?. *American Journal of Science*, 301(4–5), 313–325.
726 <https://doi.org/10.2475/ajs.301.4-5.313>

727 Whipple, K., Forte, A., DiBiase, R., Gasparini, N., & Ouimet, W. (2017). Timescales of landscape
728 response to divide migration and drainage capture: Implications for the role of divide
729 mobility in landscape evolution. *Journal of Geophysical Research: Earth Surface*, 122, 248–
730 273. <https://doi.org/10.1002/2016JF003973>

731 Willett, S. D., McCoy, S. W., Perron, J. T., Goren, L., & Chen, C. Y. (2014). Dynamic
732 reorganization of river basins. *Science*, 343, 1248765.

733 <https://doi.org/10.1126/science.1248765>

734 Willett, S.D., Slingerland, R. & Hovius, N. (2001). Uplift, shortening, and steady state topography
735 in active mountain belts. *American Journal of Science*, 301(4–5), 455–485.
736 <https://doi.org/10.2475/ajs.301.4-5.455>

737 Willis, S. C., Nunes, M., Montana, C. G., Farias, I. P., Ortí, G., et al. (2010). The Casiquiare river
738 acts as a corridor between the Amazonas and Orinoco river basins: biogeographic analysis of
739 the genus *Cichla*. *Molecular Ecology*, 19(5), 1014–1030.
740 <https://doi.org/10.1111/j.1365-294X.2010.04540.x>

741 Winemiller, K. O., López-Fernández, H., Taphorn, D. C., Nico, L. G., & Duque, A. B. (2008). Fish
742 assemblages of the Casiquiare River, a corridor and zoogeographical filter for dispersal
743 between the Orinoco and Amazon basins. *Journal of Biogeography*, 35(9), 1551–1563.
744 <https://doi.org/10.1111/j.1365-2699.2008.01917.x>

745 Xie, Y., Kang, C., Chi, Y., Wu, P., Wei, Z., Wang, J., et al. (2020). Reversal of the middle upper
746 Songhua River in the late Early Pleistocene, Northeast China. *Geomorphology*, 369(107373),
747 1–17. <https://doi.org/10.1016/j.geomorph.2020.107373>

748 Xing, Y. & Ree, R. H. (2017). Uplift-driven diversification in the Hengduan Mountains, a
749 temperate biodiversity hotspot. *Proceedings of the National Academy of Sciences*, 114,
750 E3444–E3451.

751 Yang, R., Herman, F., Fellin, M. G., & Maden, C. (2018). Exhumation and topographic evolution
752 of the Namche Barwa Syntaxis, eastern Himalaya. *Tectonophysics*, 722, 43–52. [https://](https://doi.org/10.1016/j.tecto.2017.10.026)
753 doi.org/10.1016/j.tecto.2017.10.026

754 Yang, R., Herman, F., Liu, T., Biswas, R. H., Fellin, M. G., Tian, Y., et al. (2021). Enhanced
755 Quaternary exhumation in the Namche Barwa syntaxis, eastern Himalaya. *Geology*, 49(8),
756 958–962. <https://doi.org/10.1130/G48595.1>

757 Yang, R., Suhail, H. A., Gourbet, L., Willett, S. D., Fellin, M. G., Lin, X., et al. (2020). Early
758 Pleistocene drainage pattern changes in Eastern Tibet: Constraints from provenance analysis,
759 thermochronometry, and numerical modeling. *Earth and Planetary Science Letters*, 531,
760 115955. <https://doi.org/10.1016/j.epsl.2019.115955>

761 Yang, R., Willett, S. D., & Goren, L. (2015). In situ low-relief landscape formation as a result of

762 river network disruption. *Nature*, 520(7548), 526–529. <https://doi.org/10.1038/nature14354>

763 Yanites, B. J., Ehlers, T. A., Becker, J. K., Schnellmann, M., & Heuberger, S. (2013). High
764 magnitude and rapid incision from river capture: Rhine River, Switzerland. *Journal of*
765 *Geophysical Research: Earth Surface*, 118, 1060–1084. <https://doi.org/10.1002/jgrf.20056>

766 Ye, Y., Tan, X., & Zhou, C. (2022). Initial topography matters in drainage divide migration
767 analysis: Insights from numerical simulations and natural examples. *Geomorphology*, 409,
768 108266. <https://doi.org/10.1016/j.geomorph.2022.108266>

769 Yu, X. J., Ji, J. Q., Gong, J. F., Sun, D. X., Qing, J. C., Wang, L. N., et al. (2011). Evidences of
770 rapid erosion driven by climate in the Yarlung Zangbo (Tsangpo) Great Canyon, the eastern
771 Himalayan syntaxis. *Chinese Science Bulletin*, 56, 1123–1130.
772 <https://doi.org/10.1007/s11434-011-4419-x>

773 Zeitler, P. K., Meltzer, A. S., Brown, L., Kidd, W. S. F., Lim, C., & Enkelmann, E. (2014).
774 Tectonics and topographic evolution of Namche Barwa and the easternmost Lhasa Block. In:
775 Nie, J., Hoke, G.D., Horton, B. (Eds.), *Towards an Improved Understanding of Uplift*
776 *Mechanisms and the Elevation History of the Tibetan Plateau*. Standard Performance
777 Evaluation Corporation, 507, 23–58.

778 Zeitler, P. K., Meltzer, A. S., Koons, P. O., Craw, D., Hallet, B., Chamberlain, C. P., et al. (2001).
779 Erosion, Himalayan geodynamics, and the geomorphology of metamorphism. *Geological*
780 *Society of America Today*, 11, 4–9. [https://doi.org/10.1130/1052-5173\(2001\)0112.0.CO;2](https://doi.org/10.1130/1052-5173(2001)0112.0.CO;2)

781 Zeng, X., & Tan, X. (2023). Drainage divide migration in response to strike-slip faulting: An
782 example from northern Longmen Shan, eastern Tibet. *Tectonophysics*, 229720.
783 <https://doi.org/10.1016/j.tecto.2023.229720>

784 Zhang, J. Y., Yin, A., Liu, W., Wu, F., Lin, D., & Grove, M. (2012). Coupled U-Pb dating and Hf
785 isotopic analysis of detrital zircon of modern river sand from the Yalu River (Yarlung
786 Tsangpo) drainage system in southern Tibet: Constraints on the transport processes and
787 evolution of Himalayan rivers. *Geological Society of America Bulletin*, 124, 1449–1473.
788 <https://doi.org/10.1130/B30592.1>

789 Zhang, P., Najman, Y., Mei, L., Millar, I., Sobel, E. R., Carter, A., et al. (2019). Palaeodrainage
790 evolution of the large rivers of East Asia, and Himalayan-Tibet tectonics. *Earth-Science*

791 Reviews, 192, 601–630. <https://doi.org/10.1016/j.earscirev.2019.02.003>

792 Zhao, X., Zhang, H., Hetzel, R., Kirby, E., Duvall, A. R., Whipple, K. X., et al. (2021b). Existence
793 of a continental-scale river system in eastern Tibet during the late Cretaceous–early
794 Palaeogene. *Nature communications*, 12(1), 7231.
795 <https://doi.org/10.1038/s41467-021-27587-9>

796 Zhao, X., Zhang, H., Tao, Y., Wang, Y., Pang, J., Ma, Y., et al. (2021a). Pliocene to Early
797 Pleistocene drainage reorganization in eastern Tibet inferred from detrital zircons.
798 *Geophysical Research Letters*, 48, e2021GL094563. <https://doi.org/10.1029/2021GL094563>

799 Zheng, Y., Li, H., Pan, J., Gong, Z., Wang, P., Lai, Y., et al. (2023). Mid-Pleistocene drainage
800 rearrangement of the Dadu River in response to plate convergence in southeastern Tibet.
801 *Quaternary Research*, 114, 130-147. <https://doi.org/10.1017/qua.2022.71>

802 Zhou, C., Tan, X., Liu, Y., & Shi, F. (2022a). A cross-divide contrast index (C) for assessing
803 controls on the main drainage divide stability of a mountain belt. *Geomorphology* 398,
804 108071. <https://doi.org/10.1016/j.geomorph.2021.108071>

805 Zhou, C., Tan, X., Liu, Y., Lu, R., Murphy, M. A., He, H., et al. (2022b). Ongoing westward
806 migration of drainage divides in eastern Tibet, quantified from topographic analysis.
807 *Geomorphology*, 402, 108123. <https://doi.org/10.1016/j.geomorph.2022.108123>

808 Zondervan, J. R., Stokes, M., Boulton, S. J., Telfer, M. W., & Mather, A. E. (2020). Rock strength
809 and structural controls on fluvial erodibility: Implications for drainage divide mobility in a
810 collisional mountain belt. *Earth and Planetary Science Letters*, 538, 116221.
811 <https://doi.org/10.1016/j.epsl.2020.116221>

812